May 24rd, 2025

Combined MEG and EEG suggest a limbic source network of the P3 including retrosplenial cortex and hippocampus

Diptyajit Das[a], Matti S. Hämäläinen[b], Andrew R. Dykstra[c], Andre Rupp[a], and Alexander Gutschalk[a,]*

[a] Department of Neurology, Ruprecht-Karls-Universität Heidelberg, Im Neuenheimer Feld 400,

69120 Heidelberg, Germany

[b] Department of Neuroscience and Biomedical Engineering, Aalto University School of Science, Espoo, Finland

[c] School of Communication Sciences and Disorders, University of Central Florida, Orlando, FL, USA

*** Corresponding author:**

E-mail address: Alexander.Gutschalk@med.uni-heidelberg.de (A. Gutschalk).

Abstract

The P3 is evoked by most target and salient distractor stimuli, but its neural generators have remained controversial. Here we reevaluate the role of retro-splenial cortex and hippocampus as potential generators of the P3. Combined magneto- and electroencephalography signals were recorded during a visual oddball paradigm. Observers were instructed to respond to rare targets of a deviant shape and ignore rare non-targets of a deviant color. Source analysis was based on noise-normalized minimum norm estimates in an individual, MRI-based cortical source space. Critically, the source space was extended with the hippocampus. Source analysis showed strong sources in retrosplenial cortex and hippocampus at the P3 peak. Subsequent activity was observed in insula and anterior mid-cingulate cortex. The source configuration was similar for rare target and non-target stimuli. Simulations and further analyses show that the source in retrosplenial cortex is strongly attenuated in magnetoencephalography, whereas the source in hippocampus contributes to both recording modalities. These data support that retrosplenial cortex is a main generator of the P3 in EEG and that the hippocampal P3 source can be recorded with extracranial EEG and MEG. The source configuration presented here suggests that the P3 is confined to limbic circuits.

Keywords: P300, source analysis, hippocampus, retrosplenial cortex

Abbreviations:
aMCC, anterior midcingulate cortex; CA, cornu ammonis; dSPM, dynamic statistical parametric mapping; EEG, electroencephalography; MEG, magnetoencephalography; MNE, minimum-norm estimate; ROI, regions of interest; RSC, retro-splenial cortex; S1, primary somatosensory cortex.

1 Introduction

The P3, also known as P300, is an evoked response observed for active target detection or salient, rare events (Polich, 2007; Verleger, 2020) and is one of the most studied electrophysiological brain responses in cognitive neuroscience. Using direct intracranial recordings from human epilepsy patients, P3-like activity was first found in the hippocampus (Halgren et al., 1980). Because resection of the hippocampus in such patients did not reduce the scalp P3, it was later suggested that the hippocampal P3 was generated in a closed source that is not the source of the P3 recorded with scalp electroencephalography (EEG) and with a maximum at electrode location Pz (Johnson, 1988; Onofrj et al., 1992). Later, magnetoencephalography (MEG) studies that used dipole source analysis reported that the main generator of the P3 was in the medial temporal lobe, most likely in the hippocampus (Basile et al., 1997; Rogers et al., 1993; Tarkka et al., 1995). Others proposed instead that several regions in the parietal and frontal cortex are more likely sources of the scalp P3 (Bledowski et al., 2004; Halgren et al., 1995b, 1995a; Mulert et al., 2004), and the latter interpretation was most widely accepted until today, whereas the role of hippocampus remained unclear.

By applying distributed source analysis to combined MEG and EEG (M/EEG) data obtained with an auditory oddball paradigm, Das et al (Das et al., 2024) recently suggested that the main generator of the P3 is the retro-splenial cortex (RSC). RSC activity was similarly observed in fMRI for the same participants and could well explain the maximum of the P3 response in electrode location Pz in further simulation studies. While this finding would well explain that the parietal midline P3 was not reduced by loss of the medial temporal lobe, it does not necessarily imply that the hippocampal P3 cannot be observed in other electrode or sensor locations outside of the head, as well. Moreover, the RSC is tightly connected with the hippocampus (Kobayashi and Amaral, 2007, 2003), raising interesting interpretations of the P3 at a functional level. Medial temporal lobe activity was also observed when mapping the P3 with distributed source estimation, but the authors could not rule out that this activity could be caused by mislocalized source-estimate spread from the insular or auditory cortex (Das et al., 2024). The point-spread of such source models mainly depends on the proximity and alignment (source orientation) of dipolar sources in nearby brain regions, a well-known problem when interpreting the analysis of bioelectrical signals in MEG and EEG (Hämäläinen et al., 1993; Hauk et al., 2022). Leakage from other regions is important to consider in light of the fact that another generator of the P3 has been suggested in the insular cortex (Bledowski et al., 2004; Citherlet et al., 2020; Das et al., 2024) and because activity in the auditory cortex in the P3 latency range is readily evoked by auditory oddballs even without a task (Kretzschmar and Gutschalk, 2010).

Finally, it is important to note that there are at least two variants of the P3, which have been referred to as P3a and P3b in the past: P3b is evoked by task-relevant target stimuli and shows the typical centro-parietal maximum at Pz in EEG (Hillyard et al., 1971). P3a has been reported in response to rare non-target stimuli (Squires et al., 1975) with a somewhat more anterior, central maximum at Cz. It has been suggested that novel stimuli generate yet another P3 variant (Courchesne et al., 1975; Barry et al., 2020), while others have argued that the novelty P3 and the P3a are the same evoked response (Polich, 2007). While lesions of the medial temporal lobe did not affect the P3b, as outlined above, the P3a has been shown to be strongly reduced in patients with unilateral lesions of the medial temporal lobe, while leaving an intact P3b topography (Knight, 1996).

The present study sought to further explore the generator structure of the P3 based on the following three hypotheses: First, we tested if distributed source analysis would indicate a P3 generator in the hippocampus. To this end, we used a visual instead of an auditory oddball paradigm, which anatomically mitigates spread from auditory cortex to potential sources in the hippocampus and insula. To further mitigate possible spread to these regions from auditory cortex, white noise was used to mask the sounds of button presses in response to detected targets. For the analysis of hippocampus activity, the cortical standard source space was extended to cover the full hippocampus including the cornu ammonis (CA) regions CA1-3. Second, we tested if the source in RSC – suggested by the previous auditory study (Das et al., 2024) – could be confirmed for the visual stimulus modality. Third, we similarly probed the source in insular cortex. Additionally, a distractor was added to the

stimulus paradigm to explore how the source analysis differs between target and distractor-evoked P3 responses. Further analyses were performed to explore how the MEG and EEG results compare for both, source estimates and simulations.

2 Materials and Methods

2.1 Participants

A group size of 20 participants was expected to provide robust and reliable results, since previous studies (Das et al., 2024; Doll et al., 2024) had shown converging group-level source maps with around 10 data sets, already. Accordingly, a total of 22 individuals (11 female, 11 male) between 24 and 61 years of age (mean ± standard deviation = 30.9 ± 8 years) participated in the study. None reported a history of neurological or ophthalmological disorders other than myopia. 20 participants were right-handed and two left-handed. All participants had either normal or corrected-to-normal vision, and none were color blind. Participants were students or employees recruited on campus, with no current neurological or psychiatric health issues or medication. Data from three participants were excluded due to measurement artifacts (n = 2) or co-registration errors (n = 1). Each participant gave written informed consent prior to participation, and the study was approved by the ethical council of the medical faculty at Heidelberg University.

2.2 Stimuli and experimental design

A visual oddball paradigm (Figure 1) was utilized to evoke a P3 response. The paradigm consists of two similar experimental task conditions, which were used with the intention to reduce habituation in the relatively long recording session, and which were presented in the same order to all participants. In task 1, green circles (visual angle: 1.31° x 1.31°; radius = 3.5 cm), green heptagons (visual angle: 1.31° x 1.31°; 7 sides, side length = cm, and apothem = 3.5 cm), and red circles (visual angle: 1.31° x 1.31°; radius = 3.5 cm) were presented as standard, target, and distractor stimuli. In Task 2, the standard stimuli were red squares (visual angle: 1.31° x 1.31°; radius = 3.5 cm), the target stimuli were red circles (visual angle: 1.31° x 1.31°; radius = 3.5 cm), and the distractors were green squares (visual angle: 1.31° x 1.31°; radius = 3.5 cm). All stimuli were presented with the same luminance and a refresh rate of 120 Hz in a dimly lighted environment (6.5 Lux). For each task, a total of 668 trials were presented, with the probabilities of standard, target, and distractor being 0.79, 0.12, and 0.9, respectively. Each stimulus lasted for 75 milliseconds and was presented at a regular interval of 2 s, with a jitter of ± 200 ms.

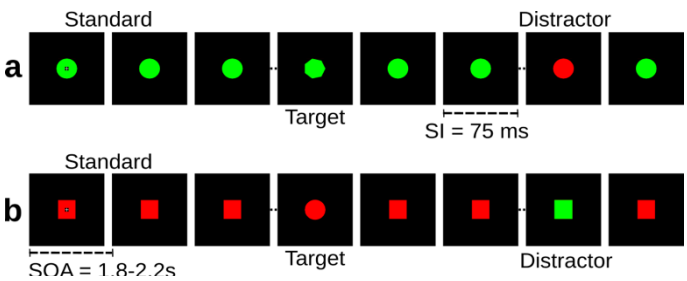

Fig. 1. Overview of the experimental design. (a) Stimulus sequence in variant 1: green circles were presented as the standard stimuli, red circles as distractor stimuli, and green heptagons served as targets. (b) Stimulus sequence in variant 2: red squares were presented as standards, red circles as targets, and the green squares were distractors. Stimuli in both variants were shown in the middle of the screen against a black background. Each stimulus lasted for a stimulus interval (SI) of 75 ms and was presented with a stimulus-onset asynchrony (SOA) of 1.8 - 2.2 s. As soon as a target stimulus appeared on the screen, participants were asked to identify it by using their right index finger to click a response button.

All stimuli were created using Psychtoolbox-3 and presented on a black background with a resolution of 1920*1080 pixels. Images were back-projected on a transparent screen mounted in a window of a magnetically shielded room (height = 31 cm and width = 35 cm), 152 cm in front of the participants, with a BenQ TK700STi projector placed outside of the magnetically shielded room. The fixation cross was initially positioned precisely at the center of the screen. Participants were instructed to

maintain their gaze on the fixation cross for the duration of each run. The participants were not instructed about the presence of distractor stimuli in the task. They were specifically told to identify only the target stimuli by clicking a response button using their right index finger as soon as a target stimulus appeared on the screen. A short break was provided in between the two tasks. Prior to each task condition, a practice session consisting of 20 trials without any distractors was undertaken to allow participants to become familiar with the task. During the experiment, constant Gaussian white noise was presented at 80 dB SPL to mask the sound produced by pressing the response button. The sound was delivered binaurally using ER-3 earphones (Etymotics Research, Elk Grove Village, IL, USA) with foam tips.

2.3 Data acquisition

The MEG recordings were conducted in a room equipped with four layers of magnetic shielding (IMEDCO AG, Hägendorf, Switzerland) during regular working hours. The recordings were performed using a Neuromag-122 whole-head system (MEGIN OY, Helsinki, Finland) comprising 61 dual-channel planar first-order gradiometers. The EEG data were obtained using a 64channel equidistant cap (Easycap, Herrsching, Germany) where the electrodes extend far down from the low cheeks until below the inion. Cz was used as a reference electrode, and the impedances of all electrodes were kept below 3 kΩ. A bipolar electrode (near the clavicle) was utilized to record the ECG (electrocardiogram) and was later used as a marker to remove cardiac artifacts from the brain signals. EEG signals were amplified using two 32-channel Neuroscan amplifiers (Abbotsford, Victoria, Australia) and sampled together with the MEG at a frequency of 1000 Hz. The positions of MEG head coils, EEG electrodes, and some additional head-shape points (~80 in total) were digitized together using the Polhemus Isotrack II digitizer (Colchester, Vermont, USA). Four head-position indicator coils were additionally digitized and used to acquire the participant's head position relative to the MEG sensors.

Anatomical 3D T1 (MPRAGE) and T2 (FLAIR) MRI scans were obtained using a 3-T Siemens Magnetom Prisma scanner (Siemens Medical Systems, Erlangen, Germany) to create an accurate boundary-element head model. MPRAGE parameters included a field of view (FOV) of 256×256×192 voxels (voxel size = 1 mm^3), repetition time (TR) = 1570 ms, echo time (TE) = 2.67 ms, inversion time (TI) = 900 ms, and flip angle = 9°. FLAIR parameters included a FOV of 192×256×25 voxels (voxel size = 0.9×0.9×5.5 mm), TR = 8500 ms, TE = 135 ms, TI = 2400 ms, and flip angle = 170°.

2.4 Data processing

Preprocessing and source estimation of MEG and EEG signals were carried out using MNE-Python (Gramfort, 2013). The raw data for each participant was visually inspected. Flat and noisy EEG channels were interpolated using the spherical spline method (Perrin et al., 1989). The oversampled temporal projection (OTP) technique was used to remove flux jumps from MEG channels (Larson and Taulu, 2018). The data were then filtered using a zero-phase finite-impulse-response (FIR) bandpass filter (0.5–30 Hz), and the EEG data were re-referenced to average reference. Next, the FastICA algorithm was used to remove cardiac artifacts and eye blinks (Hyvarinen, 1999). Epochs were obtained using time intervals of 100 ms pre-stimulus to 1 s post-stimulus. Three stimulus-driven epoch conditions were constructed during this stage: standard, target, and distractor. A separate time window of 500 ms pre-stimulus and 500 ms post-stimulus was considered to create epochs to track the response-locked brain activity. Epochs involving missed trials and false alarms were excluded from the analysis. An automatic data-driven 'autoreject' method (Jas et al., 2017) was used to repair or exclude artifact-contaminated epochs. Prior to performing source analysis, the number of epochs across experimental conditions was equalized and averaged to produce separate evoked signals per condition.

2.5 Cortex and Hippocampus surface reconstruction

Brain volume segmentation and cortical surface reconstruction for each participant was performed based on the high-resolution T1-weighted structural MRI scans using the standard stream of FreeSurfer, and individual cortex reconstructions were morphed to the spherical space of the fsaverage brain (Dale et al., 1999; Fischl, 2012). Additionally, individual participants hippocampal surfaces were derived by segmenting the bilateral hippocampus volume from each subject's T1-weighted MRI with FreeSurfer (Dale et al., 1999; Fischl, 2012). Hippocampal surfaces include subregions CA1, CA2/CA3 and CA4 on the dorsal

side, the subiculum and presubiculum on the ventral side, and a little portion of the hippocampal tail including gray and white matter on both sides (Figure 2). Topological defects such as surface-mesh distortion and vertex overlap were corrected, and surface smoothing was performed to achieve anatomically accurate surfaces suitable for M/EEG source modeling. The outer boundary of the segmented gray matter was treated as the hippocampal white-gray-matter boundary, equivalent to the white surface used in the cortex segmentation, enabling consistent surface-constrained dipole modeling in both compartments. Dipole orientations were constrained to be orthogonal to the local hippocampus surface, considering the laminar alignment of pyramidal cell populations (Palomero-Gallagher et al., 2020) as the dominant generators of the hippocampal field potentials. For group-level analyses, individual hippocampal surfaces were transformed into spherical surface representations and aligned with the fsaverage hippocampus template via a non-linear spherical registration method. Based on the hippocampal subfields, overlay matching and orthogonal dipole orientations relative to the local surface (dorsal or ventral side), two anatomical hippocampal surface labels were created. The first label corresponds to the dorsal hippocampal surface, which includes CA1–CA3 and the upper part of the hippocampal tail. The second label covers the ventral subiculum, presubiculum, and the ventral segment of the hippocampal tail.

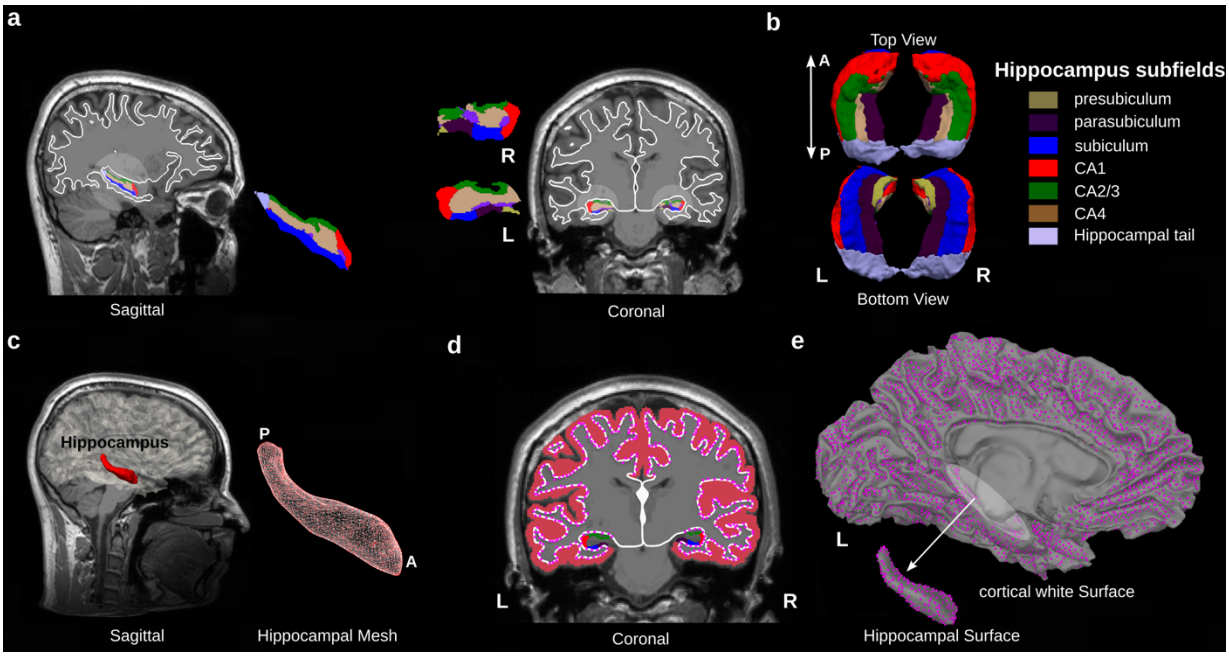

Fig. 2. Hippocampus surface reconstruction and source space. (a) The hippocampus is segmented like a nucleus at the border between the surrounding white matter and the inner gray matter (colored subfields). In contrast, cortex is segmented at the outer border of the subcortical white matter (white line). (b) In an exemplary 3D reconstruction of the complete hippocampus, the different subfields are segmented and visualized from top and bottom; this view is referenced as dorsal and ventral hippocampus in the text, respectively. The brown area labeled CA4 also includes the fusiform gyrus. (c) The 3D hippocampus surface is aligned to the cortex surface. (d) In the combined cortical and hippocampal source space, the subiculum and parasubiculum are doubled and are therefore masked in the cortical source space, together with all midline dipoles that are unrelated to cortical structures. The remaining dipoles are indicated as magenta-colored dots. In the 3D hippocampus maps, dipoles in regions CA1-3 are mostly comprised in the dorsal hippocampus view, whereas subiculum and parasubiculum dipoles are comprised in the ventral hippocampus view, the latter of which is not shown in subsequent figures. Dipoles are orthogonal to the surface and per definition point outwards from the cortex segmentation and inwards to the hippocampus segmentation. (e) Combining the two sub source spaces allows for the analysis within a continuous, unified cortical-hippocampal source space.

2.6 Source localization

The cortical white surface and the outer hippocampal surface were aligned in three-dimensional space and integrated such that the vertices and faces of the hippocampal surface extended those of the white surface in the medial temporal lobe. This extended white surface was then utilized to establish a unified source space for cortical and hippocampal sources. Participant-

specific source spaces were created by placing at least 10,242 sources (dipoles) per hemisphere at the gray-white matter boundary, with an average spacing of 3.1 mm (approx.) between the neighboring sources. Sources within the corpus callosum, and lateral ventricle wall were omitted (masked) during forward estimation using Human Connectome Project (HCP) parcellation (Glasser et al., 2016), as these regions do not include any part of the cortex. Similarly, dipoles in the subiculum complex of the cortical sub-source space were masked, because it overlapped with the ventral hippocampus sub-source space. The dipole orientation was generally from the white-gray matter boundary towards the cortical surface, i.e. outwards for the cortex sub-space and inwards for the hippocampus sub-space. For inverse modeling, three-compartment boundary-element models (BEM) were used to create participant-specific, realistic head models (Hämäläinen and Sarvas, 1989). The conductivities of the brain, skull, and skin were assumed to be 0.3 S/m, 0.006 S/m, and 0.3 S/m, respectively. Sources were assigned a loose orientation constraint (parameter value of 0.2), indicating a nearly perpendicular orientation to the cortical surface, which has been shown to improve source localization (Lin et al., 2006). A noise-covariance matrix was computed using the shrinkage technique from the 100-ms long pre-stimulus interval (Engemann and Gramfort, 2015). Combined M/EEG source estimation was performed using the linear L2 minimum-norm estimator (MNE) (Hämäläinen and Ilmoniemi, 1994; Molins et al., 2008) with noise normalization, also known as dynamic statistical parametric mapping or dSPM (Dale et al., 2000). For the group-level analysis, all individual dSPMs were transformed into the fsaverage space**.** For tasks 1 and 2, separate dSPMs were computed to account for different head positions during MEG recordings. Since these separate dSPMs produced very similar results, an average across tasks was performed to create a single dSPM solution. Later, this solution was used to show significant brain activity maps ($p < 0.01$; fixed effects). To extract local source waveforms, several regions of interest (ROI) were defined. A detailed description of ROI definitions is provided in the previously published auditory study (Das et al., 2024). In total, 5 bilateral ROIs were used, including the left and right insula, somatosensory hand area (S1), cornu ammonis (CA), retrosplenial cortex (RSC), and anterior midcingulate cortex (aMCC). Insula and RSC were directly adopted from the previous auditory study. The CA ROI was not part of the previous analysis and was based on the dorsal surface of the hippocampus. The S1 and aMCC ROIs were adjusted slightly in comparison to the previous study in order to more accurately include the activation peak of the current data set. Further information regarding this adjustment can be found in the results section. Why the activation peaks of these two ROIs did not match between the visual and auditory studies remains unclear; one possible explanation for S1 could be the utilization of different response devices. For each experimental condition, dSPM-based source time-courses for these ROIs were calculated separately by averaging the activity across all sources within each ROI using the 'mean-flip' method implemented in MNE-Python (Gramfort, 2013). This method compensates for signal cancellation by correcting the polarities of the dipoles in comparison to the average orientation produced by all dipoles for a given ROI. This process was carried out for each participant separately before producing a grand-average source time-course across the participants. Because of the restriction of our ROIs to one bank of a sulcus or gyrus, the application of the mean-flip procedure produced only minor effects and did not alter our conclusions.

Peak-latency analysis was performed on the ROI-based source time-courses to compare peak latencies for target versus distractor conditions across participants. For this procedure, the evoked signals were band-pass filtered at 1–8 Hz using a zero-phase-shift FIR filter. Peak latencies for individual ROIs were estimated within a time window between 300-700 ms after stimulus onset. Afterwards, two-sample t-tests were carried out to compare peak latencies between target and distractor P3 within each ROI. The p-values of the tests were corrected for multiple comparisons using a Bonferroni correction with an alpha level of 0.05, and only the corrected p-values ($p<0.05$) are reported.

2.7 Cortical source simulations

A simulation model was implemented to probe how well the data could be explained by a sparce source model (2.8.), and to estimate the spread between brain regions (2.9). For each participant, bilateral anatomically constrained sources were simulated based on the selected ROIs. All dipolar sources within each ROI were activated using a half-sinusoid with a base frequency of 10 Hz. The scaling of the source currents for dipoles was adjusted to ensure that the absolute mean value of all

dipoles within an ROI equaled 25 nAm at the peak activity, corresponding to the time instant with the absolute maximum amplitude. This ensures uniform source strength across ROIs, regardless of variations in their sizes. The polarity of the simulated source time-course was also adjusted with the observed polarity in the source analysis. Finally, dipoles within the left and right hemisphere ROIs were combined to create a bilateral source. This process yielded four bilateral sources: insula, CA, RSC, and aMCC, with the exception of the S1 source, where only left-hemisphere dipoles were considered to replicate contralateral, response-hand-specific brain activity. The simulated sources were then transformed back to the electrode/sensor space to produce simulated evoked signals by multiplying the simulated time-series of the sources by the gain matrix. The individual participants' noise-covariance matrices derived from the experimental M/EEG data were scaled to a total of 200 averages and added to simulated evoked signals to replicate realistic sensor-level noise.

The original, 122-chanel gradiometer MEG data were transformed into 61 virtual magnetometers using MNE-Python (Gramfort, 2013), to approximately equalize the number of MEG sensors and EEG electrodes for the least-squares procedure described in Section 2.8. Spatial maps of EEG and MEG (magnetometers) were then computed at the peak of the simulated evoked signals for each individual dataset and then averaged across all subjects to produce grand-average spatial maps for both modalities.

2.8 P3 pattern analysis using simulated sources

The activation patterns of anatomically constrained simulated sources were linearly combined to explain the P3 peak activation in experimental M/EEG data for targets and distractors. The aim of this procedure is to find a simulated activation pattern such that, when the simulated sources are multiplied by their respective weights and linearly combined, they explain the actual P3 pattern in a least-squares sense. A multiple linear regression approach (Haufe et al., 2014) was utilized here to optimize the weights from the simulated sources. This model can be expressed as:

$$\hat{y} = \sum_{i=1}^{n} x_i \omega_i \quad (1)$$

$$\hat{w} = \underset{\mathrm{w}}{\operatorname{argmin}} \, \|y - \sum_{i=1}^{n} x_i \omega_i\|_2^2 \quad (2)$$

Where, $\hat{y}$ is the predicted simulated P3 pattern; y is the actual P3 pattern; x_i is the activation pattern of the ith simulated sources; ω_i is the weight of the ith simulated source; and $\hat{w}$ are the optimal weights.

First, evoked M/EEG data were band-pass filtered at 1–8 Hz using a zero-phase FIR filter, and a search window of 300–700 ms was used for reliable P3 peak detection. P3 activation peaks were then extracted from Pz across participants to compute a grand average P3 pattern. Later, the grand-average P3 distribution is used as the target pattern (dependent variable) in the regression model. Five simulated sources (insula, S1, CA, aMCC, and RSC) were considered as the input variables (input features). Since EEG and MEG data consist of different units, z-scored standardization was performed across individual sensor types utilizing a 50-ms pre-stimulus time interval. We performed this step for both input and actual target variables, ensuring that we could compute latent weights by combining EEG and MEG data, as long as the data remained z-scored (unit-less). To achieve better uniformity, virtual magnetometer data (61 channels) are considered instead of gradiometers for MEG to maintain a similar number of MEG sensors and EEG electrodes. A multi-collinearity test was also performed to establish linear independence across input variables (simulated sources). A variance-inflation factor of 5 was observed across simulated sources during the test, meaning all the simulated sources were fairly independent from each other. Finally, to quantify the performance of the model, residual variance was calculated from the R^2 score of the model, which was calculated between the actual and predicted P3 pattern. This step was separately performed for EEG and MEG data. The optimized latent weights were multiplied by the source strength (25 nAm) of the simulated sources to provide a rough estimate of the source strength, leading to the generation of the actual P3 peak pattern in MEG and EEG.

2.9 Source leakage and sensitivity matrix

Spatial source leakage is inherent for MEG and EEG source signals due to their limited spatial resolution and the non-uniqueness of the inverse problem (Sarvas, 1987). The degree to which source leakage varies depends on the type of source estimation method being used, the sensor configurations used, source depth, and source orientation (Hauk et al., 2022). In this study,

potential leakage from and into the selected ROIs with the dSPM method were characterized using the concept of point-spread functions (PSFs) to identify source leakage. Initially, the dSPM-based resolution matrix (Samuelsson et al., 2021) for each participant was computed independently based on the simulated data. PSFs for each ROI were extracted and normalized by its maximum peak activity. Then, an average group of ROI-specific PSFs across participants was performed. Finally, an absolute Pearson correlation test was performed between the leakage activation (grand-PSFs) of one ROI and the rest of the ROIs to determine how the point-source activity from one ROI would spread to other ROIs. In this case, correlation values range from 0 to 1, where 1 signifies high leakage and 0 signifies no leakage.

In addition, the sensitivity matrix of the MEG and EEG sensor types was calculated to investigate source visibility, i.e., how the sensitivity of the sources within these ROIs would vary with respect to sensor type (but neglecting noise). First, the sensitivity matrix for each sensor type was computed by extracting the columns corresponding to normal components from the leadfield matrix for each participant. This sensitivity matrix was then morphed onto the fsaverage brain atlas, enabling the computation of a grand-sensitivity matrix across all subjects. Following this, normalization of the grand-sensitivity matrix was performed by dividing it by its maximum value. The normalized matrix was then reduced to an ROI-specific sensitivity matrix, with the values of left and right hemisphere ROIs being averaged to represent a bilateral source sensitivity matrix for individual ROIs. Sensitivity values range from 0 to 1, where 1 signifies maximum source sensitivity and 0 represents no sensitivity with respect to the sensor type.

3 Results

The data are based on a visual oddball paradigm with two non-standard stimuli. The targets were of the same color as the standards but of a different shape, and the distractors were of a different color. Participants were instructed to press a response button for the target stimuli, and to ignore the non-standard distractor stimuli. Two variants of the stimulus paradigm were used (Figure 1) with the intention to reduce response habituation. The hit rates for the two variants were similar and not significantly different across participants, with hit rates of 99.8 ± 0.67% in variant 1 and 99.3 ± 0.71% in variant 2 (mean ± standard deviation). The reaction times were 423 ± 49 ms and 425 ± 60 ms (mean ± standard deviation) in variants 1 and 2, respectively. As the separate analyses of the M/EEG data were also highly similar, the two variants were combined for the analysis presented below, to yield a better signal-to-noise ratio. The separate results for task 1 and task 2 are shown in the appendix (Figure S1).

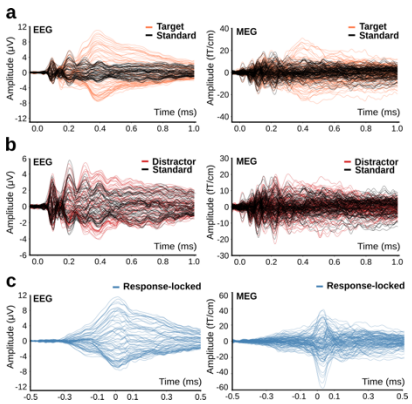

Fig. 3. Grand-average evoked signals for EEG and MEG (N=19). (a) Stimulus-locked evoked signals for EEG (left) and MEG (right) for targets (coral) and standards (black). Only the targets evoke prominent P3 activity, which occurs mostly in the 350–450 ms time range. (b) The evoked responses for distractors (red) and standards (black) are shown for EEG (left) and MEG (right). There is only a relatively weak distractor P3 observed in the range of 300 – 500 ms. Note the different amplitude scaling in a and b. (c) Evoked signals for detected targets, averaged by the button press. The somatosensory feedback is evident in MEG (right), which shows a very pronounced and rapidly growing response after the button press. In contrast, EEG (left) is dominated by a progressively increasing signal prior to the initiation of the button press.

In the grand average scalp-EEG waveforms (Figure 3, b; left panel), four subsequent peaks are observed in response to the standard stimuli, with response latencies around 100, 200, 300, and 390 ms. The target response (Figure 3a) was instead dominated by a strong P3 with a response latency of 396 ± 50 ms (mean ± standard deviation, measured at electrode Pz). The third and fourth peaks were also enhanced for the distractor stimulus (Figure 3b), but much less than for the target stimuli. We consider the fourth peak with a mean latency of 383 ± 80 ms (measured at electrode Pz) as the distractor P3 in this case. Similar responses were observed in the MEG sensor-level waveforms (Figure 3; right panel), but with somewhat less distinct P3 compared to EEG. The waveforms of the evoked response averaged relative to the time of the button responses (Figure 3c) showed peaks shortly after the button press, which were more broad-based in EEG (left) compared to MEG (right).

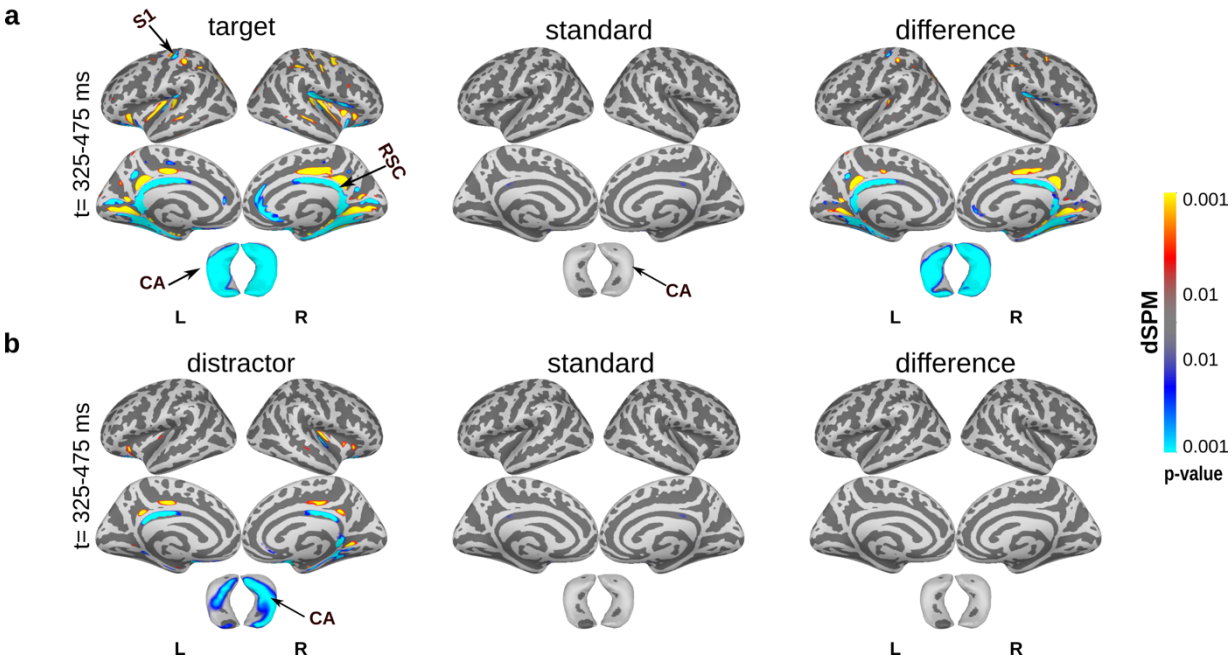

Fig. 4. Grand-average dSPM activation maps for combined M/EEG (N=19). (a) Combined M/EEG dSPM maps (p<0.01) for targets (left), standards (middle), and the contrast between targets minus standards (right) in the time window 325–475 ms after stimulus onset. (b) dSPM maps for distractor stimuli, similarly arranged. The number of trials were equalized between targets, distractors, and standards prior to source estimation. Highlighted brain regions include retrosplenial cortex (RSC), primary somatosensory cortex (S1), insula, and the cornu ammonis (CA).

Grand-average dSPM source maps of the combined M/EEG were then calculated in a time window of 325–475 ms after stimulus onset, covering the P3 peak across participants. The dSPM maps for the target stimuli (Figure 4a) first showed negative polarity in the RSC, accompanied by positive activity in two spots along the (dorsal) posterior cingulate gyrus (PCC). As has been shown before (Das et al., 2024) and is also demonstrated further below, such pairs of positive and negative-polarity on opposite sides of a gyrus are typically observed in dSPM maps with sources on one side of a gyrus. Prominent negative-going activity was also observed in the dorsal hippocampus, comprising most of CA (Figure 2). The ventral hippocampus (not shown), comprising the subiculum, revealed positive-going activity, the continuation of which is seen in some spots along the hippocampal sulcus in the cortex maps. In the more lateral convexity and in the ventral part of the parahippocampal gyrus, activity is again negative going. At the border between the medial temporal lobe and RSC clusters, activity extends into the calcarine fissure. Some midline activity was finally observed in the right anterior cingulate gyrus (ACC). On the cortical convexity, the largest cluster of activity mapped is located in the insular cortex in both hemispheres. Less prominent spots of activity are mapped to the central region and the superior temporal sulcus. Mapping the activity evoked by standards in the same time range and with the same cutoff reveals almost no activity. Accordingly, the difference between targets and standards (Figure 4a) reveals similar activity patterns in RSC and hippocampus, as observed for the

targets. Focal activity in S1 is also similarly observed in target and difference maps. Insular activity is not significant in the difference maps of the P3 peak, but is significant in a later time window (Figure S2). Similar source analysis results were obtained with the LCVM beamformer (Figure S3a) or sLORETA (Figure S3b). The maps for distractor stimuli are shown in the same arrangement in Figure 4b: Distractor maps show consistent activity in the bilateral RSC and hippocampus. Some spots of activity in the convexity are observed in insular cortex, also more prominently on the right. Neither of these activities are significant in the standard maps nor in the difference maps.

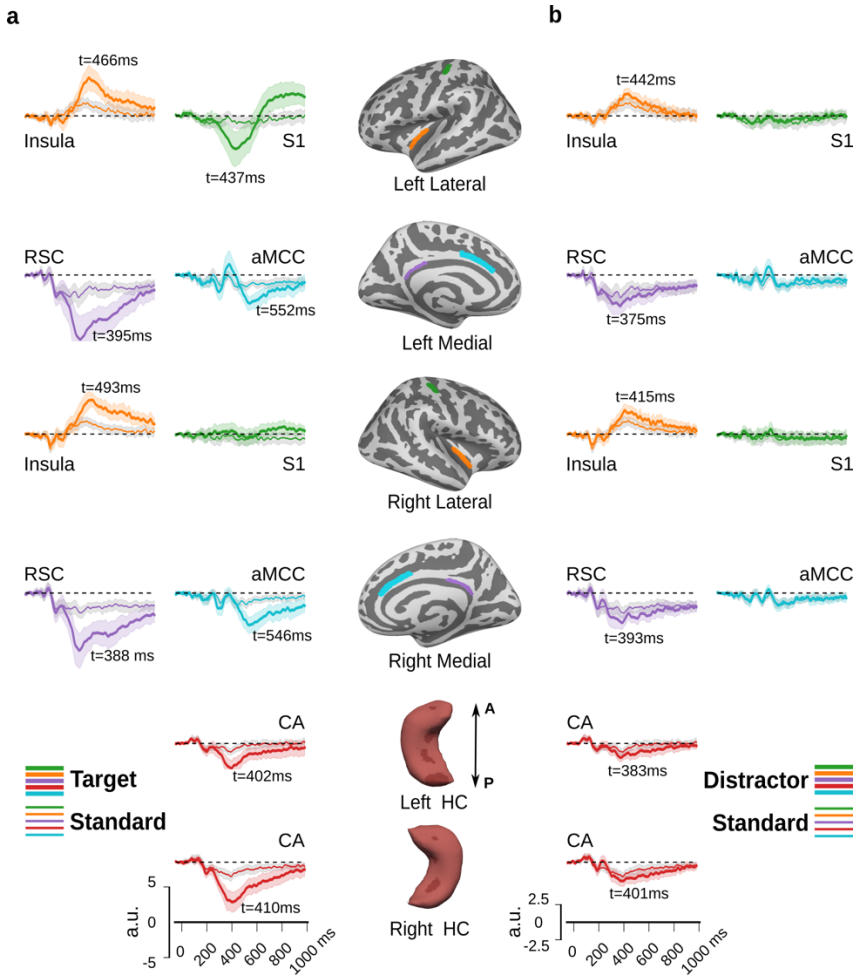

Fig. 5. ROI-based M/EEG source waveforms for target, standard, and distractor (N=19). (a) M/EEG source waveforms extracted from dSPM estimates across participants for targets (thick lines) and standards (thin lines). The ROIs are plotted in the inflated fsaverage cortex and hippocampus (middle column). The same color code is used to represent each ROI and its corresponding source waveform. The ROIs include the insula, primary somatosensory cortex (S1), retrosplenial cortex (RSC), anterior midcingulate cortex (aMCC), and cornu ammonis (CA). The shaded areas represent the 95% confidence intervals, calculated using a non-parametric bootstrap method. (b) Similar arrangement of source waveforms but for distractors (thick lines) and standards (thin lines).

The M/EEG source time courses were further evaluated in an ROI analysis (Figure 5), including previously established ROIs (Das et al., 2024) in RSC, Insula, S1, and anterior middle cingulate gyrus (aMCC). While RSC and insula were directly adopted, aMCC and S1 from our previous auditory study did not show consistent time courses with the present data. We therefore compared the dSPM maps with the previous S1 ROI and found that the peak of activity was more dorsal in the present data. Accordingly, the ROI used here was shifted more dorsal along the central sulcus. While activity in aMCC was not observed in the current maps within the P3 time window, mapping a later time window (Figure S2) reveals aMCC activity for the present data set as well. However, the activity was overall more anterior compared to the auditory study. The ROI was therefore shifted more anterior for the present analysis to allow us to image the time course of aMCC activity. An ROI in the dorsal

hippocampus (CA), covering areas CA1-3, was newly added. The source waveforms show P3-like time courses in RSC, CA, insula, and (less prominently) in aMCC. An analysis of the peak latencies for targets (Figure 6a) shows earlier latencies in RSC (443 ± 90 ms), and CA (427 ± 58 ms), and significantly longer latencies in insula (574 ± 86 ms) and aMCC (598 ± 55 ms; mean ± standard deviation). The response to distractor stimuli also showed long-latency peaks in the P3 range in RSC (391 ± 73 ms), insula (537 ± 79 ms), and CA (425± 68 ms). Compared to the target P3, however, the response to the distractors is more similar to the standard stimuli in amplitude (Figure 5b). ROI latencies are summarized in Figure 7; P3 latencies in standard, midline electrode positions are shown in Figure S4 for comparison.

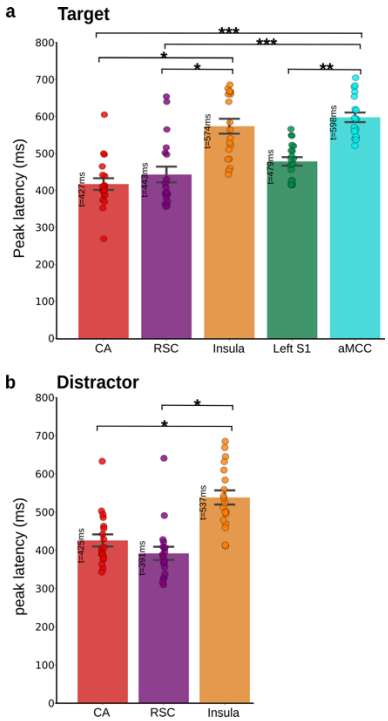

Fig. 6. Peak-latency analysis of ROI-based source time courses (mean ± standard error; N=19) for (a) targets and (b) distractors P3. The ROIs include the cornu ammonis (CA), retrosplenial cortex (RSC), insula, primary somatosensory cortex (S1), and anterior midcingulate cortex (aMCC). Significant differences between peak latencies for ROIs are indicated by asterisks (* $p < 0.05$, ** $p < 0.01$, *** $p < 0.001$) based on t-tests for repeated measures with Bonferroni correction for multiple comparison.

Next, to estimate the relative contribution of these sources, the MEG sensor and EEG scalp distribution were modeled with a linear combination of these five ROIs (Figure 7a). This model was constrained to equal source amplitudes in the left and right hemispheres for each pair of ROIs, with the exception of S1, which was only modeled in the left hemisphere. When this model was applied to the target P3 (Table 1), the strongest weighting was applied to RSC, followed by CA with about a third of the signal strengths. Activity in S1 and aMCC was yet lower, and insula received no weighting at all when all sources were used. Leaving out single sources in this model revealed that RSC explained the most variance in EEG, whereas S1 explained the most variance in MEG. Matching the overall lower residual variance in EEG compared to MEG, the maps resulting from this simulation are more similar to the original data in EEG than in MEG (Figure 7b), although the general distribution can be modeled in both modalities. A similar pattern was observed when the model was applied to the distractor P3 (Table 1; Figure 7c).

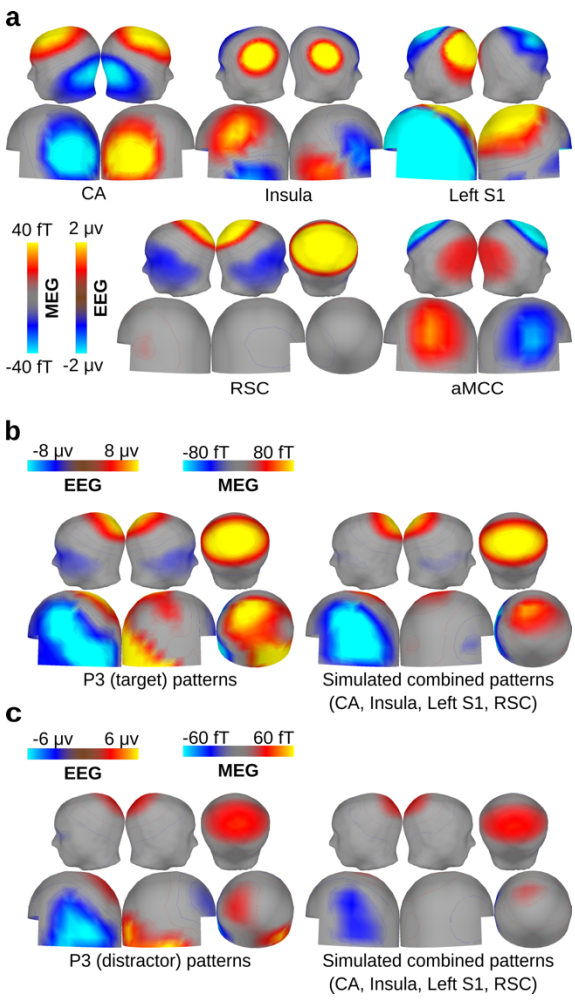

Fig. 7. Simulated M/EEG sources and sparse P3 source model. (a) Spatial pattern of scalp EEG (top) and virtual magnetometer maps (bottom) for MEG, derived from simulated sources (grand average, N=19) in the bilateral cornu ammonis (CA), insula, left primary somatosensory cortex (S1), bilateral retrosplenial cortex (RSC), and anterior midcingulate cortex (aMCC). (b) Grand-average (N=19) scalp EEG and virtual MEG magnetometer maps at the peak latency for the P3 in Pz for targets (left). Weighted (cf. table 1) combination of simulated sources in CA, insula, S1, RSC, and aMCC that best explain the P3 for targets (right). (c) Same arrangement as in b for distractor-evoked P3.

To better understand the differential role of sources for MEG and EEG, we performed a separate source analysis of the MEG (Figure 8a) and EEG data (Figure 8b). The results showed that using EEG, only, revealed overall a similar but somewhat less focused pattern compared to combined M/EEG. In contrast, MEG-only maps showed almost no activity in RSC and only minimal activity in the right insula. Only activity in CA was consistently observed in both MEG and EEG, but more anterior and right-lateralized in MEG. Activity in and around the calcarine fissure was observed in both, MEG and EEG maps. However, while the location of this activity was similar for MEG and EEG, the polarity was almost opposite, again with the EEG maps matching better with the combined M/EEG maps. The focal, negative-going activity in S1 was only observed in MEG. There was also some opposite-polarity activity around the middle cingulate cortex, which was similarly observed for MEG only, but not in the combined M/EEG.

Table 1: Relative weights and residual variance for the sparse model of the grand-average M/EEG for target P3 and distractor P3 with simulated, ROI-based sources.
CA, cornu ammonis; RSC, retro-splenial cortex; S1, primary somatosensory cortex; aMCC, anterior midcingulate cortex; EEG, electroencephalography; MEG, magnetoencephalography

Task condition	*Simulated source activation strength (nAm)*					*Residual Variance (%)*	
	CA	*RSC*	*Insula*	*Left S1*	*aMCC*	*EEG*	*MEG*
Target P3	***22.0***	***63.50***	***0.0***	***14.50***	***10.25***	***7.0***	***33.44***
	22.0	*63.50*	*-*	*14.50*	*10.25*	*7.0*	*33.44*
	13.75	*66.50*	*7.0*	*15.0*	*-*	*6.56*	*34.71*
	-	*71.0*	*5.50*	*15.25*	*0.0*	*6.96*	*40.81*
	42.75	*-*	*0.0*	*13.0*	*22.0*	*69.15*	*34.84*
	31.25	*56.75*	*0.0*	*-*	*18.50*	*13.92*	*98.04*
Distractor P3	***7.75***	***29.25***	***0.50***	***5.50***	***7.25***	***8.24***	***46.26***
	8.25	*29.25*	*-*	*5.50*	*7.50*	*8.29*	*46.14*
	10.25	*28.75*	*0.0*	*-*	*11.25*	*9.68*	*99.55*
	-	*32.5*	*5.50*	*5.75*	*0.0*	*7.42*	*52.66*
	1.5	*31.75*	*5.75*	*5.75*	*-*	*8.15*	*49.72*
	23.25	*-*	*0.0*	*5.0*	*16.0*	*72.31*	*41.04*

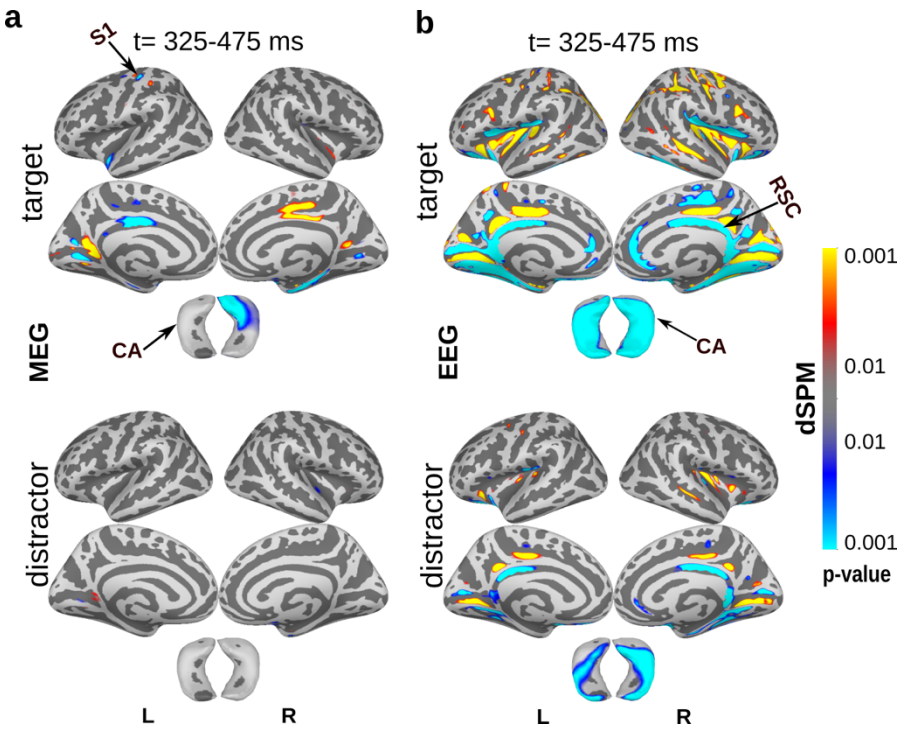

Fig. 8. Grand-average dSPM activation maps calculated separately for MEG and EEG. (a) Separate MEG and (b) EEG dSPM maps ($p<0.01$; N=19) for visual target (upper) and distractor stimuli (lower) in the time window 325–475 ms after stimulus onset. Highlighted brain regions include retrosplenial cortex (RSC), primary somatosensory cortex (S1), insula, anterior middle cingulate cortex (aMCC), and cornu ammonis (CA).

To support the interpretation of the dSPM maps and to dissociate "real" activity from source spread, we computed simulated M/EEG activity based on single-region, bilateral ROIs (except left S1) and applied dSPM source analysis for MEG and EEG only, as well as combined M/EEG (Figure 9a). Note that the scaling is normalized for the activity within the ROI used for the simulation and therefore differs between MEG, EEG, and M/EEG maps, respectively. This scaling was chosen to visualize the source spread independent of source strengths. The simulated CA activity is similarly mapped in MEG and EEG. Spread is observed to the parahippocampal gyrus in the medial temporal lobe, to the insula, and to the calcarine fissure. Spread to the calcarine fissure shows a different pattern in MEG and EEG, which shows high similarity with the pattern observed in the actual P3 maps (Figure 8). Simulated RSC activity spreads to the posterior cingulate cortex and along middle cingulate cortex. In EEG, some spread is also observed to the bilateral parietal sulci and the calcarine fissure. Simulation of insula activity shows some spread to medial temporal cortex including CA, and aMCC shows some spread towards the insula. Finally, the simulation of left-hemisphere S1 activity shows a pattern of left MCC negative (and right MCC positive activity in MEG when scaled up), which demonstrates some similarity with the MCC activity observed in the MEG-only analysis (Figure 8a). The computational analysis of spread between ROIs (Figures 9b, S5, S6, S7) confirms the visual impression, with the strongest interaction being observed between insula and CA (in particular in MEG). We finally calculated the sensitivity of MEG and EEG for the ROIs used (Figure 9c), ignoring noise. The results show that the strongest asymmetry is observed for the RSC, with a sensitivity of 0.57 in EEG and only 0.11 in MEG, consistent with the lack of RSC activity in the MEG-only analysis. Sensitivity for insula, CA, and aMCC is similar in EEG, but a factor of 1.5 higher in MEG compared to RSC. By far the strongest sensitivity is observed in S1, which is the only ROI where sensitivity in MEG almost matches EEG. Similar results are obtained when calculating the sensor-level signal-to-noise (SNR) ratio between simulated signals and physiological noise from the P3 baseline (Figure S8), where the highest signal-to-noise ratio in MEG after S1 is observed for CA and the least in RSC.

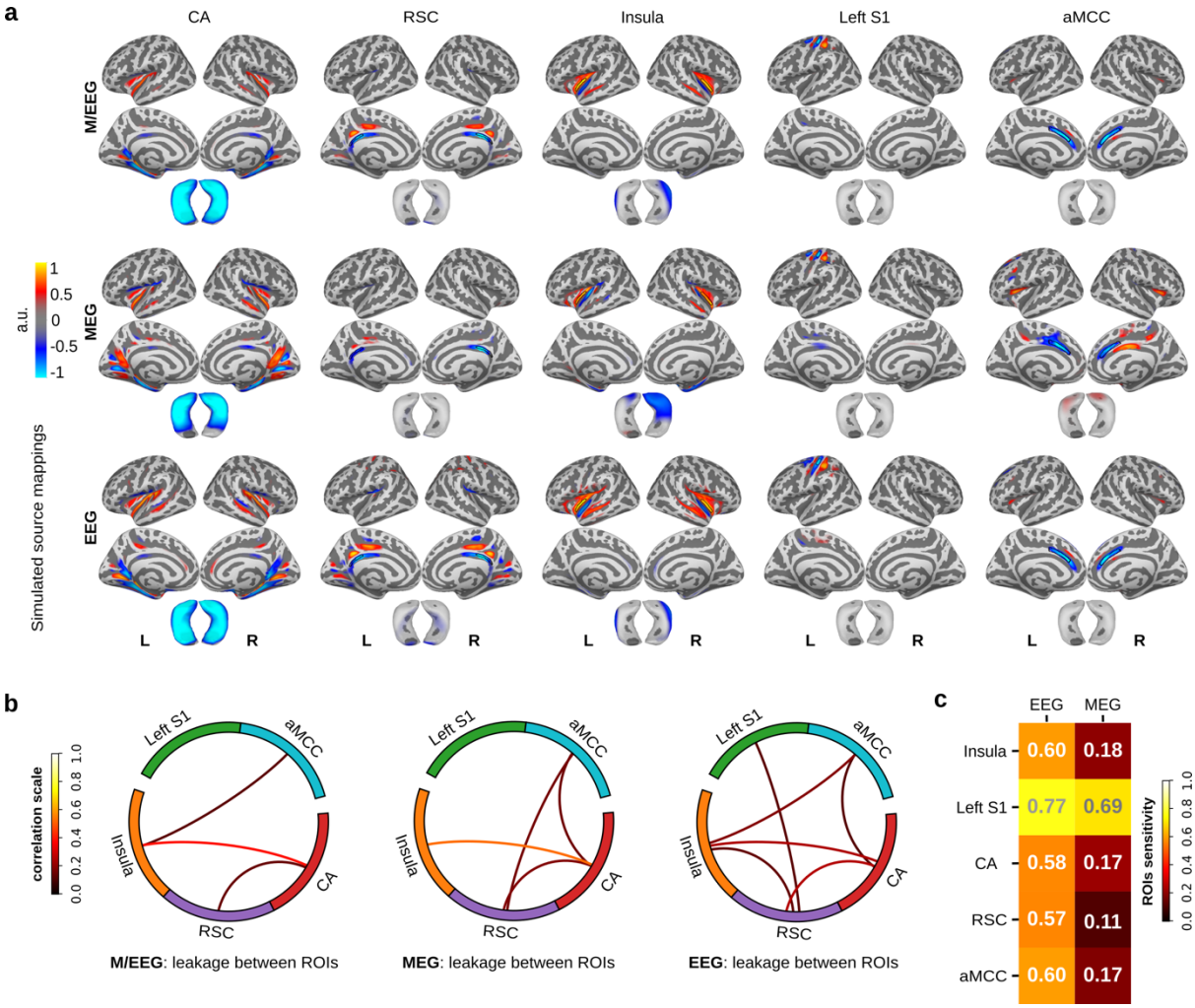

Fig. 9. Relative spatial distribution of simulated source activity when mapped similar to recorded M/EEG activity. (a) Dynamic statistical parametric maps (dSPM) for simulated M/EEG, MEG, and EEG (N=19). The maps are normalized to their peak amplitude in each ROI (i.e. the absolute cutoff is different for each single map and modality) to highlight spatial distribution rather than amplitude and signal-to-noise ratio. These maps represent simulated sources in the bilateral cornu ammonis (CA), bilateral retrosplenial cortex (RSC), bilateral insula, left primary somatosensory cortex (S1), and bilateral anterior midcingulate cortex (aMCC). (b) Point spread analysis for combined M/EEG and separate MEG and EEG, based on the simulations shown in a and illustrated with a circular graph, using a correlation cutoff value of 0.3. (c) Sensitivity matrix based on ROIs for EEG and MEG (not considering noise), with sensitivity values ranging from 0 (minimum) to 1 (maximum).

4 Discussion

These results are consistent with the notion that the P3 is predominantly generated by a set of sources that can all be classified as part of the limbic system, including in particular RSC and hippocampus. Insula and aMCC may also be active in the P3 time window, but their contribution is negative-going in frontal mid-line electrodes, rather related to the late negative wave (REF). Below we will discuss the evidence for these sources and their consequences for the functional interpretation of the P3.

Based on the data of the present study, the RSC is the dominant source of the P3 in EEG. Further support for the RSC source comes from a recent study of tone-in-noise detection (Doll et al., 2024), such that a main P3 source in RSC has now been observed with auditory (Das et al., 2024) and visual oddball tasks, as well as with a near-threshold, single-tone detection task, providing a reproduction across different paradigms and modalities. While previous experiments all used target stimuli, the

detection of which was coupled to a button press, the present data adds a distractor condition without button presses. While the amplitude of this response and, consequently, the signal-to-noise level of the source analysis, were much lower than that of the target-elicited P3, the results are nevertheless similar, suggesting a source in RSC for the distractor-elicited P3 in EEG as well. The detailed comparison of EEG and MEG provided in the present study further shows that the sensitivity of MEG is very low for an RSC source, implying that other P3 sources are more dominant in MEG.

The most prominent contributor to MEG in the P3 time-window was S1, which would not be considered a component of the P3, because it reflects activity that is clearly time-locked to the button presses in case of the target P3 (Figure S9). Unexpectedly, the sparse model fit suggests that S1 activity is also contained in the distractor P3, possibly related to actively suppressed motor responses in these no-go trials (Smith et al., 2008).

The presence of P3-like activity in hippocampus is well supported by intracranial EEG (Grunwald et al., 1999; Halgren et al., 1980; McCarthy et al., 1989; Stapleton and Halgren, 1987), and a medial-temporal-lobe source has also been suggested based on a series of MEG studies using dipole source analysis (Basile et al., 1997; Rogers et al., 1993; Tarkka et al., 1995). The finding that lesions of the hippocampus do not change the P3 in EEG (Johnson, 1988; Onofrj et al., 1992) only pertains to the prominent component at Pz. The latter finding is well explained by our source model, because Pz activity appears to be mostly generated in RSC, whereas the peak of a simulated CA source is at Fz. Because MEG is not sensitive to the RSC source, the hippocampal P3 component appears to be more prominent in MEG, instead.

The hippocampus is generally a cortical structure with parallel aligned pyramidal cells (Palomero-Gallagher et al., 2020), and the extended source model used in this paper assumes that hippocampal sources can be modeled similar to cortical sources. In analogy to neocortex, the cortical surface of the CA is on the inside of the hippocampus formation. Intracranial EEG studies consistently reported negative-going P3 activity for depth electrodes placed along the center of the hippocampal formation, with a maximum in the posterior CA (Grunwald et al., 1999; McCarthy et al., 1989; Stapleton and Halgren, 1987). While these studies also reported contacts in the subiculum, or more generally in parahippocampal gyrus, no strong activity was reported there. The orientation of the hippocampal source is expected to have some tangential component relative to the scalp surface, because it can be recorded with EEG and MEG. The average dipole orientation (normal vector) of the hippocampus ROI is towards the frontal scalp (Fz; cf. Figure 7a). Based on anatomical considerations (Iglesias et al., 2015), this hippocampal P3 source was expected to correspond more to the dorsal (rather than to the lateral) side of hippocampus, comprising mostly CA2-3 and some CA1 (cf. Figure 2).

The frontal maximum matches well with the EEG scalp distribution suggested for the P3a that was demonstrated to be reduced by unilateral medial temporal lobe lesions (Knight, 1996). The present data thus support the conclusion of Knight that the hippocampus contributes to the P3 in EEG, and in particular to the "P3a" scalp distribution. Conversely, the RSC is the main source of the parietal topography that is typically labelled as "P3b". A problem for the definition of the P3a and P3b components (Squires et al., 1975; Polich et al., 2007) is that it confounds two different scalp topographies (parietal versus frontal) with two different stimulus contexts (targets versus rare/novel distractors). However, it is obvious that the hippocampal P3 has been directly recorded with target-detection paradigms (Grunwald et al., 1999; Halgren et al., 1980; McCarthy et al., 1989; Stapleton and Halgren, 1987), which are used to obtain the P3b in scalp EEG (Polich, 2007). Based on the data presented in this paper, it appears that the RSC and hippocampal components of the P3 are present for the target and non-target P3 alike, which is well in line with the intracranial reports. It is conceivable that the hippocampal P3 is more prominent in non-target and yet stronger in novelty paradigms (Courchesne et al., 1975; Knight, 1996), shifting the maximum from Pz to Cz, or even to Fz (Polich, 2007). Such a shift of maximum can be easily demonstrated by adding simulated RSC and hippocampus activity with different relative amplitudes. An overlap of brain areas active for target and non-target stimuli has similarly been observed when target and non-target oddball stimuli were studied in fMRI (Kim, 2014).

There has been a long discussion on whether deep sources like the hippocampus can be recorded in MEG at all. The resolution to this question appears to be highly individual: Some subcortical sources like the auditory brainstem response can be recorded with MEG (Dykstra et al., 2016; Parkkonen et al., 2009) and are clearly identified not only by their source location but also by their early latency. No significant difference has been found for the sensitivity of magnetometers and gradiometers for deep sources (Hunold et al., 2016). Generally, the problem for MEG compared to EEG is not only the stronger signal drop with depth for tangential sources, but also its lack of sensitivity to radial sources (Hämäläinen et al., 1993). This is well illustrated in case of the RSC, where our simulations demonstrate the strong discrepancy in sensitivity between MEG and EEG, while for the hippocampus considerable activity is also expected in MEG based on our simulation (Figure 7a). Further support for the hippocampus being accessible to MEG comes from methodological studies (Attal and Schwartz, 2013; Krishnaswamy et al., 2017; Pizzo et al., 2019; Ruzich et al., 2019) and empirical studies of hippocampal replay (Liu et al., 2019; Wimmer et al., 2020).

One obstacle to the interpretation of the P3 dSPM maps is the consistent observation of activity in the calcarine fissure, which was observed in MEG and EEG for visual targets in the present study, but similarly with auditory targets in a previous study (Das et al., 2024). Two details lead us to suggest that this calcarine pattern in the P3 time window is spread rather than correctly located source activity. First, the polarity of the pattern is opposite in MEG- and EEG-only analyses, which is difficult to explain for a source generated directly in primary visual cortex. Second, the same pattern is observed when hippocampus activity is simulated and then mapped with the same source analysis technique, suggesting that the calcarine pattern observed in the dSPM maps may simply be spread from a hippocampal source, and, to a lesser degree, from RSC.

The other problem that cannot be resolved completely is the spread between regions that we think are all generators of the P3 network in M/EEG. This includes, but is not limited to, spread between hippocampus and insula, as well as between insula and aMCC. In the case of the insula, intracranial recordings have confirmed insular activity in the P3 latency range (Citherlet et al., 2020). We therefore think that, despite the interaction with other sources, an insular source of the P3 complex is quite likely as well. One detail of the insular P3 that remains inconsistent to the other sources is its polarity at the cortical surface. Based on the model presented here, activity in RSC is negative-going at the cortical surface, as is aMCC activity. Negative going polarity has also been observed in the hippocampus in our source analysis and consistently in intracranial studies (Grunwald et al., 1999; Halgren et al., 1980; Stapleton and Halgren, 1987). However, the insula ROI used here and in our previous auditory study (Das et al., 2024) shows positive-going polarity at the cortical surface, which is rather unlikely if the different P3 components reflected a similar cortical process. One possibility could be that we chose the wrong side of a sulcus/gyrus in our attempt to define an ROI of homogeneous polarity, but overall, activity in the insula appeared to be more positive-going. The available intracranial data recorded in the insula do not provide information to answer this question, as far as we can tell (Citherlet et al., 2020).

Beyond the question of P3 sources, which was the main focus of this paper and awaits confirmation from future work, another important question is what these sources indicate about the role in human cognition that the P3 indexes. Based on the peak latency of the sources, we found that hippocampus and RSC on the one hand, and insula and aMCC, on the other hand, have similar peak latencies. The first of these pairs, the RSC and hippocampus, have been shown to be densely and reciprocally connected (Kobayashi and Amaral, 2007, 2003). Traditionally, RSC and hippocampus have been thought to be jointly involved in episodic memory encoding and spatial navigation (Vann et al., 2009). The RSC is also thought to be generally involved in the coding of significant events (Smith et al., 2018), which could be easily linked with the presence of RSC and hippocampal P3 activity for both target and salient non-target events. The second pair, aMCC and insular cortex, are frequently coactivated during resting-state fMRI activity and are variably labeled as the ventral attention (Menon and Uddin, 2010; Thomas Yeo et al., 2011), or cingulo-opercular/insular network (Coste and Kleinschmidt, 2016; Doll et al., 2025). While RSC and hippocampal activity build up towards the button press and then decrease again, the maximum activity in aMCC showed a longer latency

after the button press. The insular latency observed in the present visual study was longer than in RSC and hippocampus and numerically earlier, but not significantly different from aMCC. This is similarly evident when source time-courses were computed for targets, averaged by the button presses (Figure S9b). Note, that insula activity was somewhat earlier in the previous auditory study (Das et al., 2024), suggesting overall that aMCC activity may succeed insular activity in latency. Moreover, the spread analysis demonstrated some interaction between insula and aMCC, which should be considered when interpreting the potential neural synchrony between these sources.

4.1 Limitations

The source analysis techniques applied in the present study have inherent limitations because of the non-unique solution of the inverse problem in a volume conductor (Hämäläinen et al., 1993). While techniques that do not have such limitation, like fMRI and iEEG, support the sources in RSC (Das et al., 2024), hippocampus (Grunwald et al., 1999; McCarthy et al., 1989; Stapleton and Halgren, 1987), and insula (Citherlet et al., 2020), we cannot exclude that further sources contribute to the P3. A number of such sources have been suggested based on fMRI and iEEG (Bledowski et al., 2004; Halgren et al., 1995b, 1995a; Mulert et al., 2004) but were not confirmed in our source analysis based on M/EEG. Alternative source configurations can therefore not be ruled out at this point. For example, it is possible that the contribution of other sources is more variable across participants and is therefore not observed in the group-level analysis used in the present study. Also, the spatial precision of M/EEG is limited, such that the exact location of the sources suggested here should be interpreted cautiously and considering that M/EEG cannot estimate the extend of a source. Finally, the analysis of the distractor P3 in the present study was only exploratory and will therefore require confirmatory studies to probe the source configuration for the P3a and P3b variants proposed above.

5 Author contributions

Diptyajit Das: Conceptualization, Experimental design, Data curation, Investigation, Methodology, Formal analysis, Visualization, Writing - original draft & editing.

Matti S. Hämäläinen: Methodology, Validation, Writing - reviewing & editing.

Andrew R. Dykstra: Validation, Writing - reviewing & editing.

Andre Rupp: Validation, Writing - reviewing & editing.

Alexander Gutschalk: Conceptualization, Experimental design, Methodology, Validation, Writing - original draft & editing, Funding acquisition, Supervision.

6 Data availability

The raw and processed MEG and EEG data and scripts will be shared upon publication and can be accessed on heiDATA, the open research data repository of Heidelberg University, Germany.

7 Declaration of interest

None of the authors have potential conflicts of interest to be disclosed.

8 Acknowledgements

This work was supported by Deutsche Forschungsgemeinschaft grant DFG 593/5-1 (AG) and by National Institute of Neurological Disorders and Stroke (NIH) grant 7R01NS104585 (MSH).

9 References

Attal, Y., Schwartz, D., 2013. Assessment of Subcortical Source Localization Using Deep Brain Activity Imaging Model with Minimum Norm Operators: A MEG Study. PLoS One 8. https://doi.org/10.1371/journal.pone.0059856

Barry, R.J., Steiner, G.Z., Blasio, F.M., Fogarty J.S., Karamacoska, D., MacDonald, B., 2020. Components in the P300: Don't forget the Novelty P3! Psychophysiology 57:e13371.

Basile, L.F.H., Rogers, R.L., Simos, P.G., Papanicolaou, A.C., 1997. Magnetoencephalographic evidence for common sources of long latency fields to rare target and rare novel visual stimuli. International Journal of Psychophysiology 25, 123–137. https://doi.org/10.1016/S0167-8760(96)00715-5

Bledowski, C., Prvulovic, D., Hoechstetter, K., Scherg, M., Wibral, M., Goebel, R., Linden, D.E.J., 2004. Localizing P300 generators in visual target and distractor processing: A combined event-related potential and functional magnetic resonance imaging study, in: Journal of Neuroscience. pp. 9353–9360. https://doi.org/10.1523/JNEUROSCI.1897-04.2004

Citherlet, D., Boucher, O., Tremblay, J., Robert, M., Gallagher, A., Bouthillier, A., Lepore, F., Nguyen, D.K., 2020. Spatiotemporal dynamics of auditory information processing in the insular cortex: an intracranial EEG study using an oddball paradigm. Brain Struct Funct 225, 1537–1559. https://doi.org/10.1007/s00429-020-02072-z

Coste, C.P., Kleinschmidt, A., 2016. Cingulo-opercular network activity maintains alertness. Neuroimage 128, 264–272. https://doi.org/10.1016/j.neuroimage.2016.01.026

Courchesne, E., Hillyard, S.A., Galambos, R., 1975. Stimulus novelty, task relevance and the visual evoked potential in man. Electroencephalogr Clin Neurophysiol 39, 131–143. https://doi.org/10.1016/0013-4694(75)90003-6

Dale, A.M., Fischl, B., Sereno, M.I., 1999. Cortical Surface-Based Analysis. Neuroimage 9, 179–194. https://doi.org/10.1006/nimg.1998.0395

Dale, A.M., Liu, A.K., Fischl, B.R., Buckner, R.L., Belliveau, J.W., Lewine, J.D., Halgren, E., 2000. Dynamic Statistical Parametric Mapping. Neuron 26, 55–67. https://doi.org/10.1016/S0896-6273(00)81138-1

Das, D., Shaw, M.E., Hämäläinen, M.S., Dykstra, A.R., Doll, L., Gutschalk, A., 2024. A role for retro-splenial cortex in the task-related P3 network. Clinical Neurophysiology 157, 96–109. https://doi.org/10.1016/j.clinph.2023.11.014

Doll, L., Dykstra, A.R., Gutschalk, A., 2024. Perceptual awareness of near-threshold tones scales gradually with auditory cortex activity and pupil dilation. iScience 110530. https://doi.org/10.1016/j.isci.2024.110530

Doll, L., Heiland., S., Gutschalk, A., 2025. A role of pupil-linked arousal, cingulo-insular cortex, and intralaminar thalamus for auditory near-threshold perception. J Cogn Neurosci, published online. https://doi.org/10.1162/jocn_a_02324

Dykstra, A.R., Burchard, D., Starzynski, C., Riedel, H., Rupp, A., Gutschalk, A., 2016. Lateralization and Binaural Interaction of Middle-Latency and Late-Brainstem Components of the Auditory Evoked Response. JARO - Journal of the Association for Research in Otolaryngology 17, 357–370. https://doi.org/10.1007/s10162-016-0572-x

Engemann, D.A., Gramfort, A., 2015. Automated model selection in covariance estimation and spatial whitening of MEG and EEG signals. Neuroimage 108, 328–342. https://doi.org/10.1016/j.neuroimage.2014.12.040

Fischl, B., 2012. FreeSurfer. Neuroimage 62, 774–781. https://doi.org/10.1016/j.neuroimage.2012.01.021

Glasser, M.F., Coalson, T.S., Robinson, E.C., Hacker, C.D., Harwell, J., Yacoub, E., Ugurbil, K., Andersson, J., Beckmann, C.F., Jenkinson, M., Smith, S.M., Van Essen, D.C., 2016. A multi-modal parcellation of human cerebral cortex. Nature 536, 171–178. https://doi.org/10.1038/nature18933

Gramfort, A., 2013. MEG and EEG data analysis with MNE-Python. Front Neurosci 7. https://doi.org/10.3389/fnins.2013.00267

Grunwald, T., Beck, H., Lehnertz, K., Blümcke, I., Pezer, N., Kutas, M., Kurthen, M., Karakas, H.M., Van Roost, D., Wiestler, O.D., Elger, C.E., 1999. Limbic P300s in temporal lobe epilepsy with and without Ammon's horn sclerosis. European Journal of Neuroscience 11, 1899–1906. https://doi.org/10.1046/j.1460-9568.1999.00613.x

Halgren, E., Baudena, P., Clarke, J.M., Heit, G., Li6geois, C., Chauvel, P., Musolino, A., 1995a. Intracerebral potentials to rare target and distractor auditory and visual stimuli. I. Superior temporal plane and parietal lobe, Electroencephalography and clinical Neurophysiology.

Halgren, E., Baudena, P., Clarke, J.M., Heit, G., Marinkovic, K., Devaux, B., Vignal, J.-P., Biraben, A., 1995b. Intracerebral potentials to rare target and distractor auditory and visual stimuli. II. Medial, lateral and posterior temporal lobe. Electroencephalogr Clin Neurophysiol 94, 229–250. https://doi.org/10.1016/0013-4694(95)98475-N

Halgren, E., Squires, N.K., Wilson, C.L., Rohrbaugh, J.W., Babb, T.L., Crandall, P.H., 1980. Endogenous Potentials Generated in the Human Hippocampal Formation and Amygdala by Infrequent Events. Science (1979) 210, 803–805. https://doi.org/10.1126/science.7434000

Hämäläinen, M., Hari, R., Ilmoniemi, R.J., Knuutila, J., Lounasmaa, O. V., 1993. Magnetoencephalography—theory, instrumentation, and applications to noninvasive studies of the working human brain. Rev Mod Phys 65, 413–497. https://doi.org/10.1103/RevModPhys.65.413

Hämäläinen, M.S., Ilmoniemi, R.J., 1994. Interpreting magnetic fields of the brain: minimum norm estimates. Med Biol Eng Comput 32, 35–42. https://doi.org/10.1007/BF02512476

Hamalainen, M.S., Sarvas, J., 1989. Realistic conductivity geometry model of the human head for interpretation of neuromagnetic data. IEEE Trans Biomed Eng 36, 165–171. https://doi.org/10.1109/10.16463

Haufe, S., Meinecke, F., Görgen, K., Dähne, S., Haynes, J.-D., Blankertz, B., Bießmann, F., 2014. On the interpretation of weight vectors of linear models in multivariate neuroimaging. Neuroimage 87, 96–110. https://doi.org/10.1016/j.neuroimage.2013.10.067

Hauk, O., Stenroos, M., Treder, M.S., 2022. Towards an objective evaluation of EEG/MEG source estimation methods – The linear approach. Neuroimage 255. https://doi.org/10.1016/j.neuroimage.2022.119177

Hillyard, S.A., Squires, K.C., Bauer, J.W., Lindsay, P.H., 1971. Evoked Potential Correlates of Auditory Signal Detection. Science (1979) 172, 1357–1360. https://doi.org/10.1126/science.172.3990.1357

Hunold, A., Funke, M.E., Eichardt, R., Stenroos, M., Haueisen, J., 2016. EEG and MEG: sensitivity to epileptic spike activity as function of source orientation and depth. Physiol. Meas. 37, 1146-1162.

Hyvarinen, A., 1999. Fast and robust fixed-point algorithms for independent component analysis. IEEE Trans Neural Netw 10, 626–634. https://doi.org/10.1109/72.761722

Iglesias, J.E., Augustinack, J.C., Nguyen, K., Player, C.M., Player, A., Wright, M., Roy, N., Frosch, M.P., McKee, A.C., Wald, L.L., Fischl, B., Van Leemput, K., 2015. A computational atlas of the hippocampal formation using ex vivo, ultra-high resolution MRI: Application to adaptive segmentation of in vivo MRI. Neuroimage 115, 117–137. https://doi.org/10.1016/j.neuroimage.2015.04.042

Jas, M., Engemann, D.A., Bekhti, Y., Raimondo, F., Gramfort, A., 2017. Autoreject: Automated artifact rejection for MEG and EEG data. Neuroimage 159, 417–429. https://doi.org/10.1016/j.neuroimage.2017.06.030

Johnson, R., 1988. SCALP-RECORDED P300 ACTIVITY IN PATIENTS FOLLOWING UNILATERAL TEMPORAL LOBECTOMY. Brain 111, 1517–1529. https://doi.org/10.1093/brain/111.6.1517

Kim, H., 2014. Involvement of the dorsal and ventral attention networks in oddball stimulus processing: A meta-analysis. Hum Brain Mapp 35, 2265–2284. https://doi.org/10.1002/hbm.22326

Knight, R.T., 1996. Contribution of human hippocampal region to novelty detection. Nature 383, 256–259. https://doi.org/10.1038/383256a0

Kobayashi, Y., Amaral, D.G., 2007. Macaque monkey retrosplenial cortex: III. Cortical efferents. Journal of Comparative Neurology 502, 810–833. https://doi.org/10.1002/cne.21346

Kobayashi, Y., Amaral, D.G., 2003. Macaque monkey retrosplenial cortex: II. Cortical afferents. Journal of Comparative Neurology 466, 48–79. https://doi.org/10.1002/cne.10883

Kretzschmar, B., Gutschalk, A., 2010. A sustained deviance response evoked by the auditory oddball paradigm. Clinical Neurophysiology 121, 524–532. https://doi.org/10.1016/j.clinph.2009.11.088

Krishnaswamy, P., Obregon-Henao, G., Ahveninen, J., Khan, S., Babadi, B., Iglesias, J.E., Hämäläinen, M.S., Purdon, P.L., 2017. Sparsity enables estimation of both subcortical and cortical activity from MEG and EEG. Proc Natl Acad Sci U S A 114, E10465–E10474. https://doi.org/10.1073/pnas.1705414114

Larson, E., Taulu, S., 2018. Reducing Sensor Noise in MEG and EEG Recordings Using Oversampled Temporal Projection. IEEE Trans Biomed Eng 65, 1002–1013. https://doi.org/10.1109/TBME.2017.2734641

Lin, F., Belliveau, J.W., Dale, A.M., Hämäläinen, M.S., 2006. Distributed current estimates using cortical orientation constraints. Hum Brain Mapp 27, 1–13. https://doi.org/10.1002/hbm.20155

Liu, Y., Dolan, R.J., Kurth-Nelson, Z., Behrens, T.E.J., 2019. Human Replay Spontaneously Reorganizes Experience. Cell 178, 640-652.e14. https://doi.org/10.1016/j.cell.2019.06.012

McCarthy, G., Wood, C., Williamson, P., Spencer, D., 1989. Task-dependent field potentials in human hippocampal formation. The Journal of Neuroscience 9, 4253–4268. https://doi.org/10.1523/JNEUROSCI.09-12-04253.1989

Menon, V., Uddin, L.Q., 2010. Saliency, switching, attention and control: a network model of insula function. Brain Struct Funct 214, 655–667. https://doi.org/10.1007/s00429-010-0262-0

Molins, A., Stufflebeam, S.M., Brown, E.N., Hämäläinen, M.S., 2008. Quantification of the benefit from integrating MEG and EEG data in minimum ℓ2-norm estimation. Neuroimage 42, 1069–1077. https://doi.org/10.1016/j.neuroimage.2008.05.064

Mulert, C., Pogarell, O., Juckel, G., Rujescu, D., Giegling, I., Rupp, D., Mavrogiorgou, P., Bussfeld, P., Gallinat, J., Möller, H.J., Hegerl, U., 2004. The neural basis of the P300 potential. European Archives of Psychiatry and Clinical Neurosciences 254. https://doi.org/10.1007/s00406-004-0469-2

Onofrj, M., Fulgente, T., Nobilio, D., Malatesta, G., Bazzano, S., Colamartino, P., Gambi, D., 1992. P3 recordings in patients with bilateral temporal lobe lesions. Neurology 42, 1762–7. https://doi.org/10.1212/wnl.42.9.1762

Palomero-Gallagher, N., Kedo, O., Mohlberg, H., Zilles, K., Amunts, K., 2020. Multimodal mapping and analysis of the cyto- and receptorarchitecture of the human hippocampus. Brain Struct Funct 225:881-907.

Parkkonen, L., Fujiki, N., Mäkelä, J.P., 2009. Sources of auditory brainstem responses revisited: Contribution by magnetoencephalography. Hum Brain Mapp 30, 1772–1782. https://doi.org/10.1002/hbm.20788

Perrin, F., Pernier, J., Bertrand, O., Echallier, J.F., 1989. Spherical splines for scalp potential and current density mapping, Electroencephalography and clinical Neurophysiology. XXX

Pizzo, F., Roehri, N., Medina Villalon, S., Trébuchon, A., Chen, S., Lagarde, S., Carron, R., Gavaret, M., Giusiano, B., McGonigal, A., Bartolomei, F., Badier, J.M., Bénar, C.G., 2019. Deep brain activities can be detected with magnetoencephalography. Nat Commun 10. https://doi.org/10.1038/s41467-019-08665-5

Polich, J., 2007. Updating P300: An integrative theory of P3a and P3b. Clinical Neurophysiology. https://doi.org/10.1016/j.clinph.2007.04.019

Rogers, R.L., Basile, L.F., Papanicolaou, A.C., Eisenberg, H.M., 1993. Magnetoencephalography reveals two distinct sources associated with late positive evoked potentials during visual oddball task. Cereb Cortex 3, 163–9. https://doi.org/10.1093/cercor/3.2.163

Ruzich, E., Crespo-García, M., Dalal, S.S., Schneiderman, J.F., 2019. Characterizing hippocampal dynamics with MEG: A systematic review and evidence-based guidelines. Hum Brain Mapp. https://doi.org/10.1002/hbm.24445

Sämann, P.G., Iglesias, J.E., Gutman, B., Grotegerd, D., Leenings, R., Flint, C., Dannlowski, U., Clarke-Rubright, E.K., Morey, R.A., van Erp, T.G.M., Whelan, C.D., Han, L.K.M., van Velzen, L.S., Cao, B., Augustinack, J.C., Thompson, P.M., Jahanshad, N., Schmaal, L., 2022. FreeSurfer-based segmentation of hippocampal subfields: A review of methods and applications, with a novel quality control procedure for ENIGMA studies and other collaborative efforts. Hum Brain Mapp. https://doi.org/10.1002/hbm.25326

Samuelsson , J.G., Peled, N., Mamashli, F., Ahveninen, J., Hämäläinen, M.S., 2021. Spatial fidelity of MEG/EEG source estimates: A general evaluation approach. NeuroImage 224:117430.

Sarvas, J., 1987. Basic mathematical and electromagnetic concepts of the biomagnetic inverse problem. Phys Med Biol 32, 11–22. https://doi.org/10.1088/0031-9155/32/1/004

Shaw, M.E., Hämäläinen, M.S., Gutschalk, A., 2013. How anatomical asymmetry of human auditory cortex can lead to a rightward bias in auditory evoked fields. Neuroimage 74, 22–29. https://doi.org/10.1016/j.neuroimage.2013.02.002

Smith, D.M., Miller, A.M.P., Vedder, L.C., 2018. The retrosplenial cortical role in encoding behaviorally significant cues. Behavioral Neuroscience 132, 356–365. https://doi.org/10.1037/bne0000257

Smith, J.L., Johnstone, S.J., Barry, R.J., 2008. Movement-related potentials in the Go/NoGo task: The P3 reflects both cognitive and motor inhibition. Clinical Neurophysiology 119, 704–714. https://doi.org/10.1016/j.clinph.2007.11.042

Squires, N.K., Squires, K.C., Hillyard, S.A., 1975. Two varieties of long-latency positive waves evoked by unpredictable auditory stimuli in man. Electroencephalogr Clin Neurophysiol 38, 387–401. https://doi.org/10.1016/0013-4694(75)90263-1

Stapleton, J.M., Halgren, E., 1987. Endogenous potentials evoked in simple cognitive tasks: depth components and task correlates. Electroencephalogr Clin Neurophysiol 67, 44–52. https://doi.org/10.1016/0013-4694(87)90162-3

Tarkka, I.M., Stokić, D.S., Basile, L.F., Papanicolaou, A.C., 1995. Electric source localization of the auditory P300 agrees with magnetic source localization. Electroencephalogr Clin Neurophysiol 96, 538–45. https://doi.org/10.1016/0013-4694(95)00087-f

Thomas Yeo, B.T., Krienen, F.M., Sepulcre, J., Sabuncu, M.R., Lashkari, D., Hollinshead, M., Roffman, J.L., Smoller, J.W., Zöllei, L., Polimeni, J.R., Fischl, B., Liu, H., Buckner, R.L., 2011. The organization of the human cerebral cortex estimated by intrinsic functional connectivity. J Neurophysiol 106, 1125–1165. https://doi.org/10.1152/jn.00338.2011

Uutela, K., Taulu, S., Hämäläinen, M., 2001. Detecting and Correcting for Head Movements in Neuromagnetic Measurements. Neuroimage 14, 1424–1431. https://doi.org/10.1006/nimg.2001.0915

Vann, S.D., Aggleton, J.P., Maguire, E.A., 2009. What does the retrosplenial cortex do? Nat Rev Neurosci 10, 792–802. https://doi.org/10.1038/nrn2733

Verleger, R., 2020. Effects of relevance and response frequency on P3b amplitudes: Review of findings and comparison of hypotheses about the process reflected by P3b. Psychophysiology 57. https://doi.org/10.1111/psyp.13542

Wimmer, G.E., Liu, Y., Vehar, N., Behrens, T.E.J., Dolan, R.J., 2020. Episodic memory retrieval success is associated with rapid replay of episode content. Nat Neurosci 23, 1025–1033. https://doi.org/10.1038/s41593-020-0649-z